ELSEVIER

Contents lists available at ScienceDirect

Computer-Aided Design

journal homepage: www.elsevier.com/locate/cad



NURBS-based microstructure design for organic photovoltaics*,**



Ramin Noruzi, Sambit Ghadai, Onur Rauf Bingol, Adarsh Krishnamurthy*, Baskar Ganapathysubramanian*

Mechanical Engineering, Iowa State University, Ames, IA, USA

ARTICLE INFO

Article history: Received 8 May 2019 Received in revised form 1 August 2019 Accepted 22 September 2019

Keywords: NURBS Microstructure modeling Organic solar cells Voxelization Interface modeling Optimization

ABSTRACT

The microstructure - spatial distribution of electron donor and acceptor domains - plays an important role in determining the photo current in thin film organic solar cells (OSCs). Optimizing the microstructure can lead to higher photo current generation, and is an active area of experimental research. There has been recent progress in framing OSC microstructure design as a computational design problem. However, most current approaches to microstructure optimization are based on volumetric distribution of material, which makes the design space very large. In contrast, we frame the microstructure design optimization problem in terms of designing the interface between the donor and acceptor regions, and thus pose it as a surface representation and optimization problem. This results in substantially reduced number of design variables, thus enabling use of standard optimization tools. In this work, we address the efficient design of OSC microstructure by using surface and curve modeling techniques to model the donor-acceptor interface, and use meta-heuristic, gradient-free optimization techniques to optimize the microstructure for maximum short circuit current generation. Our modeling framework consists of three major components: (1) geometric modeling of OSC microstructure that uses Non-Uniform Rational B-spline (NURBS) curves and surfaces to construct the free-form donor-acceptor interface, (2) photo-current generation modeling that uses a parallel, finite-element based excitondrift-diffusion (XDD) model, and (3) optimization that utilizes genetic algorithms (GA) to optimize the OSCs microstructure via exploration of the NURBS representation. We apply these methods for the optimization of both 2D and 3D microstructures. Results show substantial improvement in current density compared to the bulk-heterojunction microstructures. These results provide promising microstructures for experimental groups to fabricate. The proposed surface representation approach seems to be a promising approach for interface design in engineered systems.

© 2019 Elsevier Ltd. All rights reserved.

1. Introduction

In the last two decades, numerous studies have investigated the chemistry of materials used in organic solar cells (OSCs) in order to enhance the photocurrent generation. These advances along with limited process optimization have helped improve OSC efficiency from less than 1% to over 10% [1]. The community believes that additional improvements in efficiency are possible by rationally tailoring the morphology or the microstructure of the OSC [2]. This is very promising because OSCs exhibit several

E-mail addresses: noruzi@iastate.edu (R. Noruzi), sambitg@iastate.edu (S. Ghadai), orbingol@iastate.edu (O.R. Bingol), adarsh@iastate.edu (A. Krishnamurthy), baskarg@iastate.edu (B. Ganapathysubramanian).

advantages over their inorganic counterparts, that make them very attractive for diverse applications. These advantages include (a) significantly reduced cost in comparison to traditional inorganic photovoltaics [3], (b) natural structural flexibility, allowing for easier transport and installation [4], (c) easy tunability to achieve diverse colors and textures, and (d) production of devices with unusual form factors, thus extending their applicability to consumer electronics.

OSCs are typically thin films that are comprised of two types of organic materials (i.e. molecules containing a carbon backbone) called electron donor and electron acceptor (excitons). The spatial distribution of the donor and acceptor domains in the thin film (i.e. microstructure) is critical to the performance of the device. This is because each stage of the photocurrent generation process – light absorption, exciton generation, exciton dissociation, and charge transport – is directly affected by the microstructure. Fig. 1 shows a schematic view of a thin film OSC. The incident solar radiation causes excitons (which are electron–hole pairs) to form in the electron donating region. The excitons dissociate into positive and negative charges at

 $[\]stackrel{\dot{}}{
m iny}$ This paper has been recommended for acceptance by Gershon Elber.

ቱቱ No author associated with this paper has disclosed any potential or pertinent conflicts which may be perceived to have impending conflict with this work. For full disclosure statements refer to https://doi.org/10.1016/j.cad. 2019.102771.

^{*} Corresponding authors.

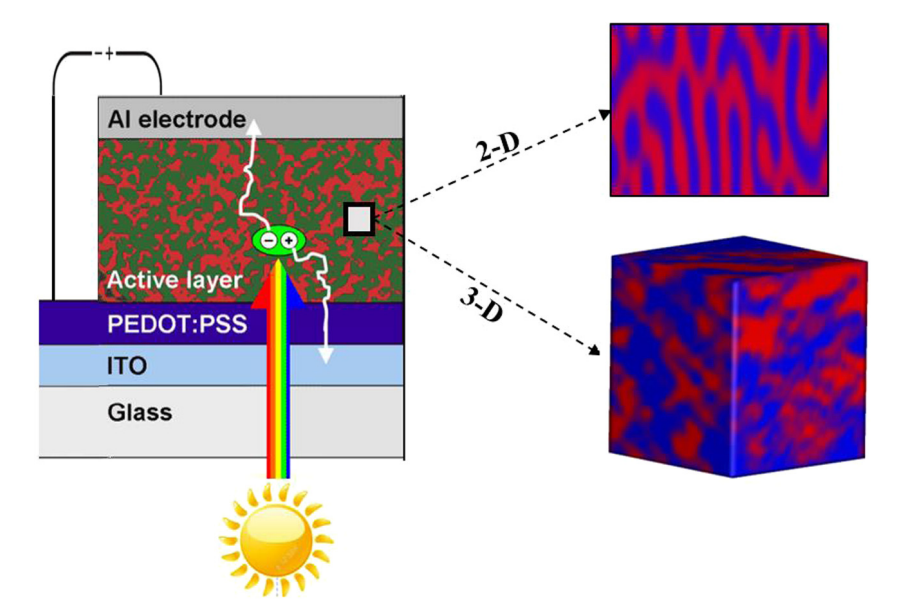


Fig. 1. Schematic of the current generation process in a typical organic solar cell. The active layer is made of a blend of acceptor and donor materials. A representative volume element (RVE) of this active layer is represented by the microstructure. The active layer is composed of repeating 2D or 3D unit RVEs.

the donor–acceptor interface. These charges then travel through the domain – positive charges through the electron donor, and negative charges through the electron acceptor – to reach the top and bottom electrodes, thus producing current. Each stage of the photo-current generation process (exciton creation, exciton dissociation, charge transport) is affected by the underlying microstructure, thus making a compelling argument for rational design of OSC microstructure.

Microstructure-sensitive design has been successfully used in applications focused on bulk behavior such as the field of elastic/structural materials [5]. However, microstructure design is still a nascent topic when other applications - especially multiphysics applications - are considered. This is especially true in the context of studies seeking to improve the performance of OSC's. Recent work on modeling the microstructure-aware photophysics has finally resulted in the availability of simulation tools that can map a given microstructure to its photovoltaic performance. One such set of tools model the photo-physics via the exciton-drift-diffusion (XDD) equations, which are a set of tightly coupled partial differential equations. Using these simulation tools, there have been recent studies [6,7] that seek to understand the effect of specific microstructural features on the device performance [8,9]. However, there have been very few studies to *design* the microstructure. This research gap motivates the current work.

Various design approaches have been developed in the field of microstructure sensitive design [10–12]. These approaches include: (1) modeling materials and geometry separately using voxel-based methods [13], (2) utilizing implicit modeling methods to model both the geometry and the material composition [14], and (3) decomposing the microstructure into several sub-objects, each of which refers to a different material class and combining them using Boolean operations [15]. However, even though these methods are promising for manual microstructure design, they many not be the most efficient choices for microstructure design through optimization. This is because these methods are based on volumetric distribution of material, which makes the design space very large.

In this work, we frame the microstructure design optimization problem in terms of designing the interface between the donor and acceptor regions (DA interface), and thus pose microstructure

design as a surface representation and optimization problem. This novel approach results in substantially reduced number of design variables, thus enabling use of sophisticated optimization tools to improve the short-circuit photocurrent generation. We utilize a NURBS-based interface generation method that uses NURBS curves or surfaces to represent the donor-acceptor interface within a representative volume element (RVE). We develop and deploy an automated workflow that takes in a NURBS curve or surface, find its envelope (bounded by the curve or surface), and use rasterization methods to convert the RVE into a binary volumetric representation. We then solve the XDD equations for this RVE to assess its performance (i.e. short-circuit current production). An optimization framework uses this performance evaluation to modify the DA interface to obtain higher performance. We demonstrate this workflow in both 2D and 3D by identifying promising classes of microstructures with improved performance.

This paper is arranged as follows: we explain the physics model in Section 2. We then explain the motivation behind representing the microstructure using the Donor–Acceptor interface in Section 3. We then detail our approach for 2D and 3D microstructure modeling and optimization in Sections 4 and 5, respectively. We present a comprehensive discussion of the results in Section 6 and conclude in Section 7.

2. Physics model: Microstructure to property mapper

The microstructure of an OSC thin film consists of two materials spatially distributed in the domain. The spatial distribution, $m(\vec{x})$, of the two materials (called electron-donor and electron-acceptor) determines the photovoltaic performance of the OSC. Without loss of generality, we can represent a microstructure as a binary image (or volume), or equivalently as a two-phase material [16]. There are broadly two approaches to computationally interrogate a microstructure, $m(\vec{x})$, to evaluate its photovoltaic performance: (1) microscopic/discrete models and (2) continuum/PDE models. Microscopic models, usually based on (kinetic) Monte Carlo approaches, can accurately describe the effect of microstructure on charge generation, recombination, and transport. They have been used with great utility to understand the effects of various sub-processes in semiconductor

device operations. However, these methods are computationally very expensive to use for three-dimensional simulations and high throughput analysis, thus precluding them as viable options for microstructure design. Continuum models based on the drift-diffusion equations [17–20], provide a computationally efficient alternative to microscopic models. Continuum models can also incorporate recombination, exciton generation, and creation of free charges unique to the physics of OSC device operation. The effect of microstructure is incorporated into the drift-diffusion model by using spatially-varying material properties based on the spatial distribution of constituent materials, both in 2D [20–22] and in 3D [22].

We, therefore, use an Exciton-Drift-Diffusion model (XDD) to evaluate the performance of a microstructure. A detailed discussion of the XDD equations is provided in Appendix A. We briefly outline the basic photo-physics that the equations model. The exciton equations (X) models the generation, diffusion, dissociation of excitons in the domain. The incident solar radiation is absorbed by the electron donor regions resulting in a volumetric generation of excitons. The excitons diffuse towards the donoracceptor (DA) interface, where they undergo dissociation into an electron and hole. The kinetics of this dissociation (k_d) depends on the local density of charges (n, the electron density and p, the hole density). The drift-diffusion equations model how these charges (n, and p) are transported across the domain to the respective electrodes. This consists of two phenomena: diffusion of charges from high density regions to low density regions, and the drift of the charges under the imposed electric field. Additionally, the charge densities interact with each other via Columbic attraction undergoing recombination. All these phenomena are accounted for in the XDD equations.

The XDD equations are solved using a stabilized finite element approach [22] along with the imposition of weak boundary conditions [23]. An in-house parallel FEM framework [22,24] is used to solve the XDD equations.

3. Microstructure interface representation using parametric curves/surfaces

A standard way to represent the microstructure, $m(\vec{x})$, is using a field, i.e. a spatial distribution where $m(\vec{x})$ takes a value of 1 when \vec{x} lies in phase one, and takes a value 0 when \vec{x} lies in phase two. This representation is essentially an indicator function representation at every spatial location. While simple and intuitive, this results in a very large design space for microstructure design.

We utilize a key feature of the photo-physics to reformulate the microstructure representation into an equivalent form that exhibits a much more compact parameterization. As described in the previous section, the exciton dissociates into an electron and hole pair at the donor-acceptor interface. For successful collection of these pair of charges, the electron must successfully traverse through the acceptor domain to reach the bottom electrode, while the hole must successfully traverse through the donor domain to reach the top electrode. The presence of any isolated islands (of either material) will result in loss of viable pathways of charges from that region to the appropriate electrode, producing a degradation in performance. Thus, it has been argued that good morphologies exhibit a bi-continuous structure [5]. A bi-continuous structure is defined as a structure in which two contiguous phases interpenetrate. Thus, for every point, \vec{x}_{DA} , on the donor-acceptor interface, there exist continuous pathways from \vec{x}_{DA} through the acceptor domain (i.e. $m(\vec{x}) = 1$) to one electrode, **and** through the acceptor domain (i.e. $m(\vec{x}) = 0$) to the other electrode. A bi-continuous structure ensures that every part of the DA interface is viable (see Fig. 2). We emphasize that this is a necessary (but not sufficient) condition for maximal

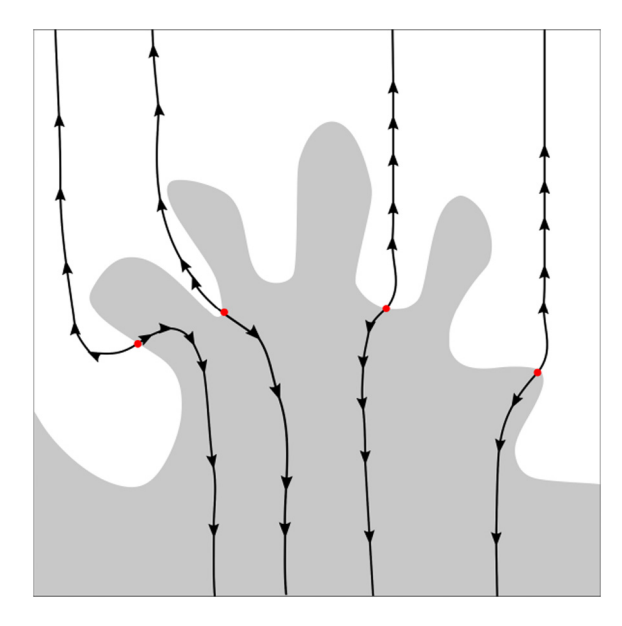


Fig. 2. Illustration of a bi-continuous morphology. The red dots are representative points on the donor-acceptor interface, and the directed lines represent pathways from the DA interface to the respective electrodes.

extraction of charges. It is very interesting to note that standard processing approaches for OSC produce BHJ morphologies that exhibit a nearly bi-continuous morphology [25].

We, thus, seek to optimize two-phase microstructure that exhibit a *bi-continuous* property. Such microstructures are uniquely defined by the *interface* between the two phases. The microstructure is fully defined by a non-intersecting boundary that defines the interface between the two distinct components. It follows that the mathematical tools for parametric representation of curves (in 2D) and surfaces (3D) can be effectively utilized to characterize the interface, and thus the microstructure.

This is a critical insight as it converts the computationally difficult problem of **volumetric** microstructure design into a more tractable **surface** design of the interface. We emphasize that this reformulation is not specific to the OSC microstructure design problem we consider here, but is endemic to a wide variety of material systems – including catalysis, energy harvesting, and membranes – where a bi-continuous property is expected. Moreover, multiple manufacturing techniques produce such microstructures [26], making the designs realizable.

Representing the interface using a curve or surface that exhibits a *bi-continuous* property necessitates that the boundary is not self intersecting. This can be handled in two ways: (1) carefully parameterizing the interface to prevent self-intersections for all possible interfaces in the design space, or (2) detecting and removing self-intersections after the interface has been generated. Both these methods are computationally tractable for a 2D microstructure design. Hence, we implemented both these approaches in this work for 2D microstructure optimization (see Section 4). On the other hand, detecting and removing self-intersections in 3D surface representations is much more challenging. We resolve this challenge by computing the (lower) envelope of the NURBS surface using ray intersection methods and directly voxelizing the microstructure (see Section 4).

We frame the design problem as an surface optimization problem and use genetic algorithms (GAs) as the optimization routine. GAs have been proven to be successful in many scientific applications where computing the derivatives is not possible or challenging. We utilize the curve/surface reformulation for microstructure design and illustrate the methodology first in 2D and

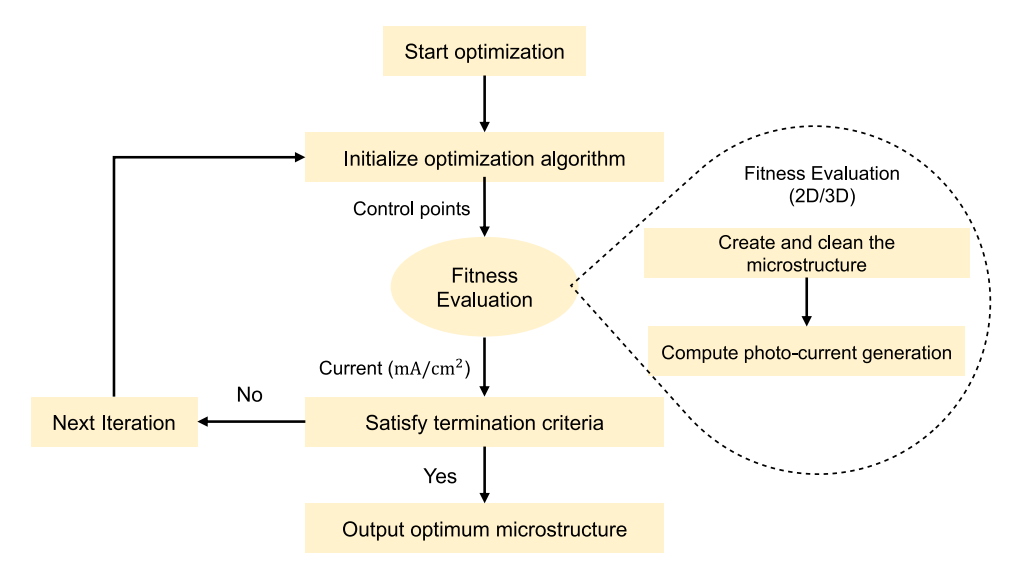


Fig. 3. Overall workflow for using genetic algorithms for optimization of microstructure of OSCs. The fitness evaluation step (magnified in the inset) for 2D and 3D microstructures is explained in detail in Sections 4 and 5, respectively.

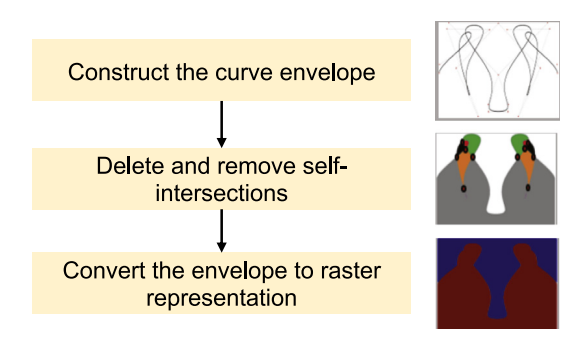


Fig. 4. The algorithm for 2D microstructure design.

then in 3D. Fig. 3 shows the optimization framework of current study using GAs.

4. Microstructure modeling: Formulation and results for the 2D case

For the 2D microstructure, we model the donor–acceptor interface using NURBS curves, detect and remove the self intersections, and use rasterization methods to convert the resulting RVE into a volumetric (image pixel) representation. In the volumetric representation, the RVE is divided into a user-defined grid of pixels and each pixel is classified into acceptor or donor regions. Thus each representation of the interface can be converted directly into a microstructure.

Fig. 4 shows the three steps to create a 2D microstructure. In the first step, we use curve modeling techniques to construct the interface curves using NURBS. In the second step, we detect and eliminate self intersection(s). In the third step, we find the lower envelop of the curve to convert into a raster (volumetric) representation.

4.1. Curve modeling

The coordinates of a parametric curve is defined with respect to a parametric value. Consider $\mathbf{g}:[a,b]\to R^s$ for $s\geq 2$, this mapping is called a parametric representation of class C^m for $m\geq 1$ if it satisfies the following conditions. First, all the n components of \mathbf{g} should have continuous derivatives up to

order m and second, the first derivative of \mathbf{g} should not vanish in [a, b],

$$D\mathbf{g}(t) = \mathbf{g}'(t) \neq 0, \text{ for } t \in [a, b]$$
 (1)

Note that a function y = f(x) can always be considered as a curve through the parametric representation f(u) = (u, f(u)). In this paper we use this property to represent the DA interface as a curve in 2D and as a surface in 3D. Non-uniform rational B-splines (NURBS) are a superset of curve/surface representation that we use to represent the donor–acceptor interface in our work. Detailed equations of NURBS curves can be found in Piegl and Tiller [27]; in the following we review NURBS equations briefly.

NURBS curves: The NURBS curve is a parametric curve that can be represented using control points (P), weights (w), and the knots (U). P forms the control polygon and U should form a sequence of non-decreasing numbers. In other words knot vector should be formed such that:

$$U = \{u_0, \dots, u_p, u_{p+1}, \dots, u_{m-p-1}, u_{m-p}, \dots, u_m\}$$
 (2)

where, $u_i \leq u_{i+1} (i=0,\ldots,m-1)$. The number of knots in u direction is m+1. Without loss of generality, the NURBS curve is defined the parametric domain u=[0,1]. As a consequence, $u_0=0$ and $u_m=1$.

The B-spline basis functions $N_{i,p}(u)$ on U are defined recursively such that:

$$N_{i,0}(u) = \begin{cases} 1 & \text{if } u_i \leqslant u < u_{i+1} \\ 0 & \text{otherwise} \end{cases}$$

$$N_{i,p}(u) = \frac{u - u_i}{(u_{i+p} - u_i)} N_{i,p-1}(u) + \frac{u_{i+p+1} - u}{(u_{i+p+1} - u_{i+1})} N_{i+1,p-1}(u)$$
(3)

By having $N_{i,p}(u)$ we can define the NURBS curve as a function of the parameter u as:

$$C(u) = \frac{\sum_{i=0}^{n} N_{i,p}(u) w_i P_i}{\sum_{i=0}^{n} N_{i,p}(u) w_i}$$
(4)

We can define piece-wise rational functions $(R_{i,p}(u))$ such that

$$R_{i,p}(u) = \frac{N_{i,p}(u)w_i}{\sum_{j=0}^{n} N_{j,p}(u)w_j}$$
 (5)

Therefore Eq. (4) can be rewritten as

$$C(u) = \sum_{i=0}^{n} R_{i,p}(u) P_i \tag{6}$$

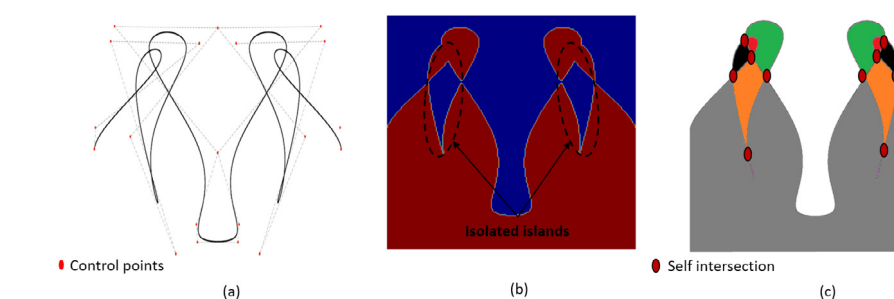


Fig. 5. Schematic representation of detection and elimination of self-intersection(s).

There are many advantages associated with using NURBS curve for the interface. Some of the NURBS characteristics that are related to this study are:

- 1. NURBS have a local control property. From $R_{i,p}(u) = 0$ for $u \notin [u_i, u_{i+p+1})$, we can conclude that moving a single control point P_i only affects the piece of the NURBS curve which $u \in [u_i, u_{i+p+1})$ and not outside this interval.
- 2. The general shape of the NURBS curve C(u) is determined by the control polygon formed by the convex hull of control points from P_{i-p} to P_i while $u \in [u_i, u_{i+1})$.

We model the DA interface using NURBS with a new approach for the parameterization. Most of the studies in the literature assume that the control points are distributed linearly along x-axis but are free to move only along the y-axis (for example see [28]). This assumption avoids self intersection and generating the interface envelope is trivial using the ray-casting algorithm. However, allowing the control points to move only in 1 direction can be too restrictive to create optimal microstructures. Hence, in our approach, we allow the control points to move freely in both x and y axes. This assumption creates more realistic microstructures, since the generated curves have more degrees of freedom. However, in this case, there could be self-intersections, which need to be specially handled to generate the curve envelope.

4.2. Detection and elimination of self-intersection(s)

Evaluating the self intersection of NURBS curves is an essential operation in the design of microstructure since it can have direct impact on the performance of the OSCs [29]. Given a general curve C(t) as is presented in Fig. 5(a), the microstructure result shown in Fig. 5(b) is not the one typically desired since it has multiple isolated islands. Presence of isolated islands increases the recombination of carrier charges which decreases current generation of the device dramatically. As a result, the self-intersections in the resulting computed curve are expected to be trimmed away. In order to detect self intersections, we subdivide C(t) into monotone linear regions, and then processes all the (monotone) segments using a plane sweep scheme. For this purpose, we use Bentley and Ottmann algorithm [30] which is a sweep-line algorithm to find all k intersections among n line-segments with an $\mathcal{O}((n+k)\log n)$ time complexity. Following are detailed steps for this algorithm.

- 1. Let there be n given line segments. There must be 2n end points corresponding to these n lines. Sort all points according to x coordinates.
- 2. Tag a flag to each point indicating whether this point is left point of its line or right point.
- If the current point is a left point of its line segment: Check for intersection of its line segment with the segments just above and below it. And add its line to active line segments.

4. If the current point is a right point of its line segment: Remove its line segment from active list and check whether its two active neighbors intersect with each other.

(d)

Note that steps 3 and 4 are like passing a vertical line from all points starting from the leftmost point to the rightmost point.

Once an intersection is detected, the curve is split at this location. Our method for removing self-intersection(s) is based on the physics of OSCs. As we mentioned before, isolated islands decrease current generation of OSCs dramatically, as a result, we eliminate those set of line segments which create these type of islands in the final microstructure. Fig. 5(a) shows the curve envelope generated by NURBS and Fig. 5(b) shows corresponding microstructure for this curve. It can be seen that there are multiple isolated islands in this figure. Fig. 5(c) shows detection of intersection and segments of Fig. 5(a). Fig. 5(d) shows the corresponding microstructure for Fig. 5(a) after elimination of intersecting regions. The microstructure in Fig. 5(d) has 380% more current generation compared to the microstructure in Fig. 5(b).

4.3. Conversion to volumetric representation

Once the envelope is constructed, we convert this representation back into a volumetric representation, $m(\vec{x})$. We construct a lattice of points in the domain (depending on the mesh density required for solving the photophysics equations (see next section). For each point on the lattice, we evaluate the phase it lies on to create $m(\vec{x})$. We use ray-casting algorithm to find the phase of each point. Briefly, this method works based on the number of times a ray, starting from the point and going in any fixed direction, intersects with the envelope of the curve. If the point is on the inside (outside) of the envelope the ray will intersect it an odd (even) number of times. This algorithm is computationally inexpensive and fast, however, it may not work correctly for complex geometries with self intersection(s). Thus, our previous step of detection and elimination of self-intersection(s) is an essential step to maintaining the accuracy of this step.

4.4. Microstructure optimization using genetic algorithms

We use our XDD model to assess the performance of a microstructure and use it to frame the optimization problem: Find the NURBS parameters that result in a 2D microstructure with maximal short circuit current. Numerical explorations revealed that the cost-function can be highly corrugated making computing of the gradient non-trivial. Additionally, numerically computing the gradient is computationally expensive (as the solution of the XDD equations are themselves computationally expensive). Finally, we impose shape constraints which makes parts of the design space out of bounds. Based on these characteristics, we choose to use a meta-heuristic, gradient free, optimization strategy. We specifically use a genetic algorithm (GA), as we have prior

experience in utilizing this class of approaches for optimizing complex engineered systems [31].

There are many variants of GA, however, we describe the standard algorithm below:

- 1. Initialize the first generation of points with randomly generated points in the search space. These points are encoded into strings and are called "chromosomes".
- Evaluate each chromosome of this generation using a fitness function that best relates to the problem. Here the fitness function is the short circuit current computed by solving the XDD equations. Rank order the chromosomes based on fitness value.
- 3. Select chromosomes based on their fitness to create a new generation of individuals through crossover and mutation methods. Good fitness is rewarded by an increased possibility of selection. To create the next generation, there are three standard methods:
 - Crossover combines genetic material (i.e. specific design variables) in an individuals' chromosomes and creates offsprings that maintain some of the traits of the parents. A crossover rate decides the portion of each new generation that should come from crossover.
 - Mutation randomly alters the bits within a chromosome. This initiates a random variation into the population which potentially brings prospective solutions out of local optima.
 - A set of top-performing chromosomes in the population are selected as 'elites', whose chromosomes are retained in the next generation. This maintains the optimal solution across the GA.
- 4. Repeat steps 2–3 until some set of termination criteria are met, usually:
 - Stall generation limit: Terminate the GA if optimal or mean fitness fails to improve for a set number of generations.
 - Generation limit: Terminate the GA if a set number of generations are explored.
 - Stall time: Terminate the GA if the runtime for the GA reaches a set value.

An optimal solution is determined by choosing the most efficient individual chromosome within the final generation. In this work, the GA is formulated as a minimization problem which makes lower fitness more desirable. Because GAs utilize a population of potential solutions distributed over the design space, they are less likely to getting stuck in local minima. Please note that GA is a stochastic optimization method, so it is expected that running it multiple times will produce different results. One practical way to solve this issue is repeating each optimization multiple times. This gives us the opportunity to observe statistical significance of results and reliably explore the phase space.

Design variables, simulation time and assumptions: We model donor–acceptor interface with NURBS. Since each set of control points represents a unique microstructure, we identify the control points as the design variables. Some questions which arise here are: how many control points are needed in order to generate a microstructure? What are the diversity of generated microstructures with NURBS? We address these questions below:

Accuracy and computational costs are two major concerns of this current work. Usage of more control points models donoracceptor interface with higher order curves and ultimately constructs more complex microstructures. However, this also increases the computational complexity of the optimization process

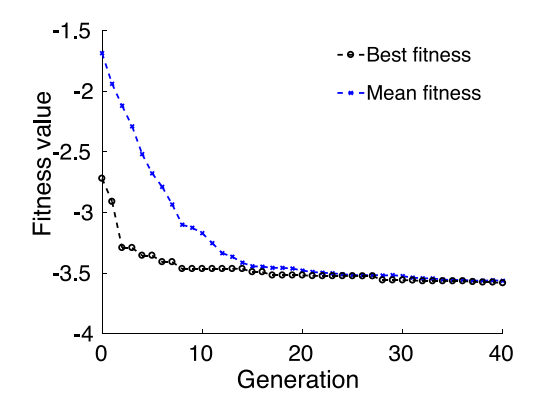


Fig. 6. Convergence study of GA.

dramatically. This is because of the nature of the governing PDEs – exciton–drift–diffusion equations – which are highly nonlinear. Approximately, each fitness function requires about an hour for evaluation on a HPC cluster with one node (16 processors). As a result, finding the minimum number of control points – which creates microstructures which are reasonably complex, yet require reduced computational cost – is a crucial step in the design process.

Principle component analysis (PCA) is a convenient way to investigate the diversity of generated data. To understand the diversity of the microstructures, we generated different microstructures using NURBS with 4, 8, 16, and 32 control points. We then performed PCA on the microstructure images, took the top two values (i.e. map each image to a point in 2D), and visualized them (see Fig. 7). As expected, microstructures created using larger number of control points have more diversity than those created with fewer number of control points. However, increasing number of control points from 16 (green zone) to 32 (red zone) does not cause a significant increase in the microstructure diversity. In order to quantify this claim, we computed the area enclosed by the convex hull of blue (microstructures generated using 4 control points, A₁), black (microstructures generated using 8 control points, A_2), green (microstructures generated using 16 control points, A_3) and red points (microstructures generated using 32 control points, A_4). Quantitatively, $A_2/A_1 = 2.265$, $A_3/A_2 =$ 1.189, and $A_4/A_3 = 1.015$. This shows changing the number of control points from 16 to 32 does not significantly change the area occupied by the corresponding points. As a result, we choose NURBS with 16 control points and uniform knot vector to model the microstructure.

Problem Constraints: The constraints in this problem were driven by the geometric characteristics of the microstructure. For simplicity and without loss of generality we assume that the microstructure has a unit length in x and y direction. Generated curves should therefore satisfy: $y_{max} < 1$ and $y_{min} > 0$, $y_{max} < 1$ and $y_{min} > 0$. Consequently, a set of control points $y_{min} > 0$ are valid only if the curve produced satisfy Eq. $y_{min} > 0$. The same constraints are extended to 3D for the 3D microstructure generation.

$$0 \le \Sigma_{i=0}^n R_{i,p}(u) P_i \le 1 \tag{7}$$

GA convergence: As we discussed earlier, GAs are an inherently stochastic method, so we repeat each optimization multiple times (20 times) to consider statistical significance of results and attempt to reliably explore the phase space. However, there is no guarantee that we can find the global minima. This is however not a major problem in design as we seek to identify microstructures that are better performers than our current best. Fig. 6 shows the convergence of GA for this problem.

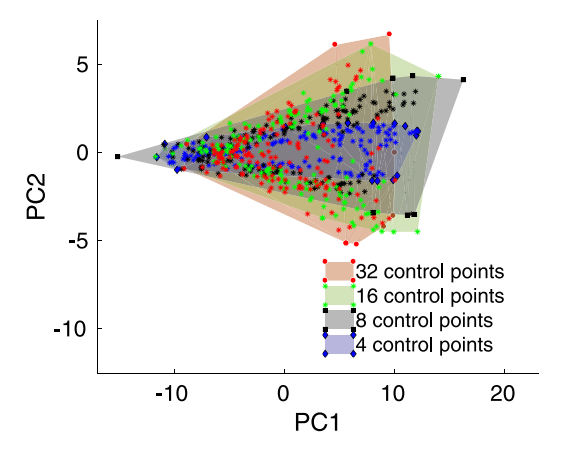


Fig. 7. Dimension reduction of microstructures created by NURBS by mapping each microstructure image to a unique point in xy-plane. Blue, gray, green and red zones represent diversity of generated microstructures with 4, 8, 16 and 32 control points respectively. (For interpretation of the references to color in this figure legend, the reader is referred to the web version of this article.)

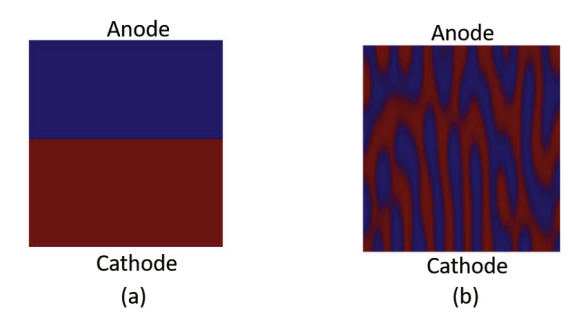


Fig. 8. 2D microstructure (a) bilayer and (b) bulk heterojunction (BHJ), red shows electron acceptor regions and blue shows electron donor regions. (For interpretation of the references to color in this figure legend, the reader is referred to the web version of this article.)

4.5. Simulation parameters

Genetic operators and parameters: In the present study, stochastic uniform selection, intermediate crossover, and adaptive feasibility were selected as the parameters of the GA. The size of population and maximum evolution generation are set to 50 and 200, respectively. The optimization process is terminated if there is a low chance to achieve significant changes in the next generations i.e. when relative error between two generations is less than a specified criteria. The maximum allowable relative change of fitness function is set to 0.001. Eq. (8) shows termination condition of GA.

$$\frac{\|f_{best}(i) - f_{best}(i-1)\|}{\|f_{best}(i-1)\|} \le 0.001$$
(8)

OSC device parameters: In this paper we consider a device with thickness of 100 nm fabricated using P3HT:PCBM donoracceptor blend. The material specific parameters for this system were obtained from Kodali [22]. The device configuration is such that the electrodes are placed at the top and bottom boundaries (in 2D) and side boundaries (in 3D). In all cases, the microstructure image clearly identifies the surfaces that act as cathode and anode.

4.6. Optimized microstructure

With the model system detailed in the previous section, we use GA to find microstructures with high short circuit current. We compare charge transport properties of the optimized microstructure with bilayer and bulk heterojunction (BHJ) microstructures. We choose these two microstructures for comparison as their properties have been widely studied [32,33]. Fig. 8 shows the 2D microstructure of bilayer and BHJ. We note that most current high performance OSC devices have been shown to exhibit a BHJ microstructure. The bilayer microstructure is included as a comparative reference since the first successful OSC was made from stacking together two layers. Current OSC – with BHJ microstructures – have substantially larger short circuit currents compared to the bilayer microstructure, primarily due to their higher donor–acceptor interfacial area.

Consequently, we use the current density of BHJ, denoted (J_{ref}), as a reference metric to compare our optimization results with. This value is $J_{ref}=1.319~\text{mA/cm}^2$. Since our analysis is not limited to a specific polymeric system, we choose to express the current density of optimized microstructures as a ratio of the current density of the BHJ structure i.e. current density is scaled by J_{ref} .

Fig. 9 shows the optimized microstructure designed using NURBS 2D. The value of collected current is $J/J_{ref}=2.914$ i.e. short-circuit current was improved by about 190% compared to 2D BHJ structure. Fig. 9(a) and (b) show the contour of the electron and hole current densities components normal to the electrodes.

5. Microstructure modeling: Formulation and results for the 3D case

We explained the required steps to design 2D optimized microstructures in the previous section. In this section, we explain how we extend the same methodology to design 3D optimized microstructures using NURBS surfaces. Note that the physical model, optimization method and simulation parameters are the same for both 2D and 3D cases.

5.1. NURBS surface interface generation

To represent the microstructure in 3D, we first create a NURBS surface that represents the DA interface, similar to the 2D example. This is done by generating a set of 16 control points, 4 in each dimension, for the microstructure surface. The boundary points of the control points mesh are clamped on to the x-ymid-plane for uniformity. Using these control points mesh and the NURBS-Python spline library [34], we generate a bi-cubic NURBS surface using automatically-generated uniform knot vectors in all parametric dimensions. The resulting NURBS surface is tessellated and exported as a triangle soup (a Wavefront .obj representation file) for further computations. An example of this is shown in Fig. 11(a). We use this surface to create a solid boundary representation (B-rep) watertight model of the microstructure. We create four orthogonal side faces, which along with the x-y plane and the clamped NURBS surface forms a closed solid object, since the edges of the NURBS surface are clamped to the x-y mid-plane. This is illustrated in Fig. 11(b) with a wireframe visualization of the triangle mesh. This triangle mesh or the B-rep model of the solid is further voxelized to generate a volume representation of the microstructure as explained in the next section.

5.2. Voxelization-based envelop generation

The B-rep model of the 3D microstructure is generated as mentioned in the previous section. We then compute the envelope of this 3D surface and rasterize the microstructure for the simulations. For this purpose, it is necessary to classify whether

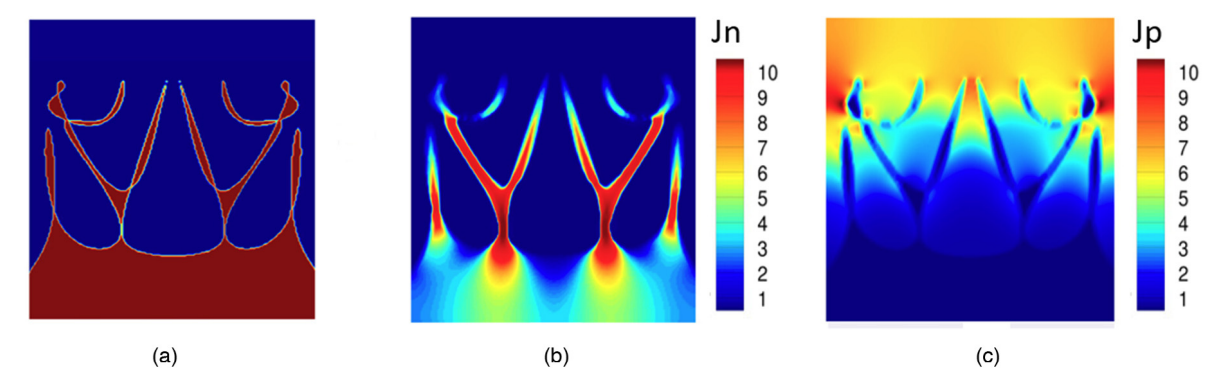


Fig. 9. Optimized microstructure design using NURBS 2D. (a) Microstructure, red shows electron acceptor regions and blue shows electron donor regions. (b) Normal component of electron current density. (c) Normal component of donor current density. (For interpretation of the references to color in this figure legend, the reader is referred to the web version of this article.)

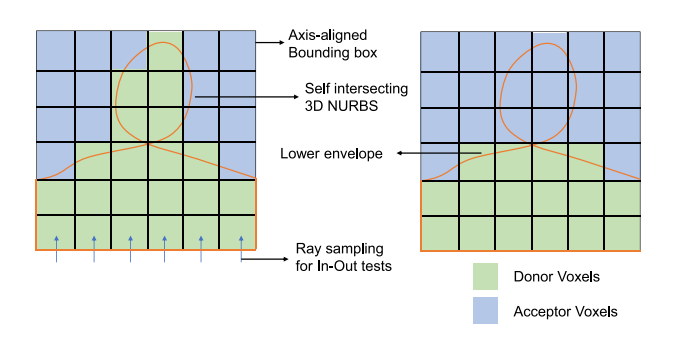


Fig. 10. Illustration of self intersecting 3D NURBS resolved through lower envelope after inside-outside classification during voxelization.

a point is inside (acceptor region) or outside (donor region) the solid microstructure. In order to compute the point membership classification of the solid, we convert the B-rep model of the microstructure to a volume representation using a structured voxel grid and a ray-casting algorithm. Using the GPU-accelerated Voxelization framework by Young and Krishnamurthy [35], we generate the volume occupancy grid based on whether a voxel representing the grid lies inside the volume or outside the volume. The complete voxel grid is a binary grid of in(1) and out(0)representing the acceptor region and donor region of the microstructure, respectively. An example of a microstructure represented as a B-rep model and an In-Out voxel model is shown in Fig. 12. We first represent the NURBS surface as a pseudomanifold solid model by converting it to a dense set of triangles. We then voxelize the triangle mesh to compute the lower envelope. This prevents the problem of self intersecting surfaces as the ray-tracing algorithm with odd-even intersections of the boundary correctly computes the in and out of the geometry by computing the first intersection. The lower envelope is computed by using only the first intersection of each ray and discarding any other subsequent intersections (see Fig. 10). This ameliorates the issue of wrong inside-outside classification with self-intersecting surfaces. The special case when a ray intersects exactly with the self-intersection curve on the surface is handled using an antialiasing approach. We compute the intersection using 4 adjacent rays (similar to 2×2 anti-aliasing) and use the intersection outcome of the majority (2) of the rays for computing the lower envelope. This method overcomes the need to compute the selfintersection of NURBS surfaces. The disadvantage is that multiple NURBS surfaces might produce the same microstructure, but the optimization process can overcome this issue, since what we are interested is the optimized microstructure.

5.3. Optimized microstructure

Similar to 2D design, we compare charge transportation properties of the optimized microstructure in 3D with bilayer and bulk heterojunction (BHJ). Fig. 13 shows the microstructure of bilayer and BHJ. We apply exciton–drift–diffusion model in 3D to the above mentioned structures and evaluate their electricity generation. 3D BHJ has a higher donor–acceptor interfacial contact area which results in a higher electricity generation compared to bilayer. We use current density of 3D BHJ (J_{ref}) as a reference metric. We obtained the value of reference current density as $J_{ref} = 1.289 \, \text{mA/cm}^2$

Fig. 14 shows the optimized 3D microstructure designed with NURBS surfaces. The value of collected current is $J/J_{ref}=2.454$ i.e. short-circuit current was improved by 145% compared to 3D BHJ structure. Current density of electron and hole is shown in Fig. 14(b) and (c). The electron current-density is negligible in the electron-donor area and increases in the acceptor area from anode to cathode. A comparable effect is detected with hole current-density. In the following section, we discuss the two optimized microstructures.

6. Discussion of the results: Interpretation and detailed characterization of the optimized microstructures

Fig. 15 illustrates a comprehensive performance comparison of 2D optimized microstructure with bilayer and BHJ. According to Fig. 15, electricity generation of bilayer and BHJ are $J_{bilayer} =$ 1.210 mA/cm² and $J_{BHI} = 1.319$ mA/cm² while the current density of 2D optimized microstructure is $J_{optimized} = 3.843 \text{ mA/cm}^2$. Thus, the optimized 2D microstructure produces 3.17 and 2.91 times useful current compared to the bilayer and BHJ devices, respectively. Fig. 15 also compares dissociation (D) and recombination (R) rates of above mentioned microstructures. In general more dissociation and less recombination leads to a higher amount of current generation. According to contours of (D) and (R) in Fig. 15, bilayer has least amount of dissociation and recombination, BHJ have a higher amount of dissociation and recombination but there is a good balance between amount of dissociation and recombination for the optimized microstructure resulted in a higher electricity generation for this microstructure.

Similarly, Fig. 16 depicts performance comparison of 3D optimized microstructure with bilayer and BHJ. According to Fig. 16, electricity generation of bilayer and BHJ are $J_{bilayer} = 0.980 \text{ mA/cm}^2$ and $J_{BHJ} = 1.289 \text{ mA/cm}^2$ while the current density of 3D optimized microstructure is $J_{optimized} = 3.158 \text{ mA/cm}^2$. Thus, the current generated by the optimized 3D microstructure is 3.22 and 2.44 times that generated by the bilayer and BHJ devices, respectively.

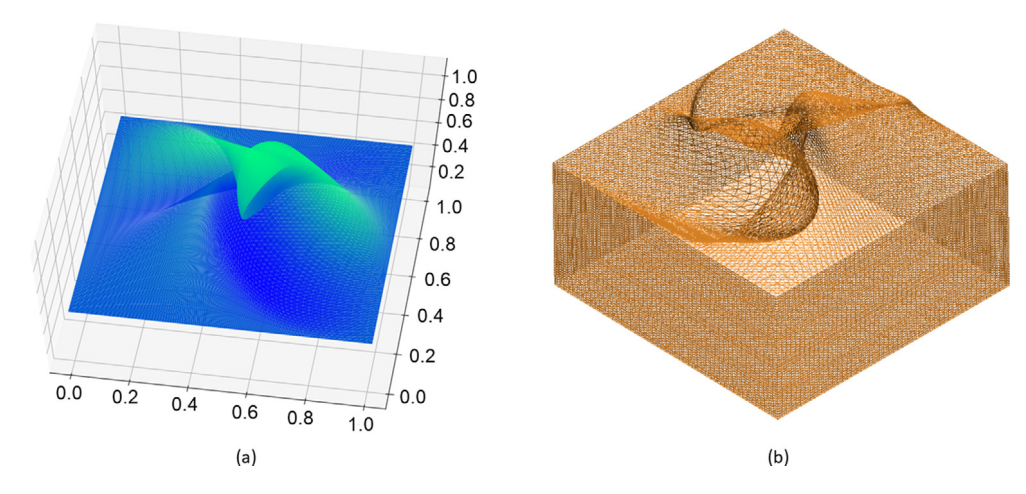


Fig. 11. (a) NURBS surface representation modeled with 16 control points. Control points have been distributed evenly among x-axis and y-axis and they have random z-coordinates. (b) NURBS surface with closed boundaries that generates a pseudo-manifold B-Rep solid model.

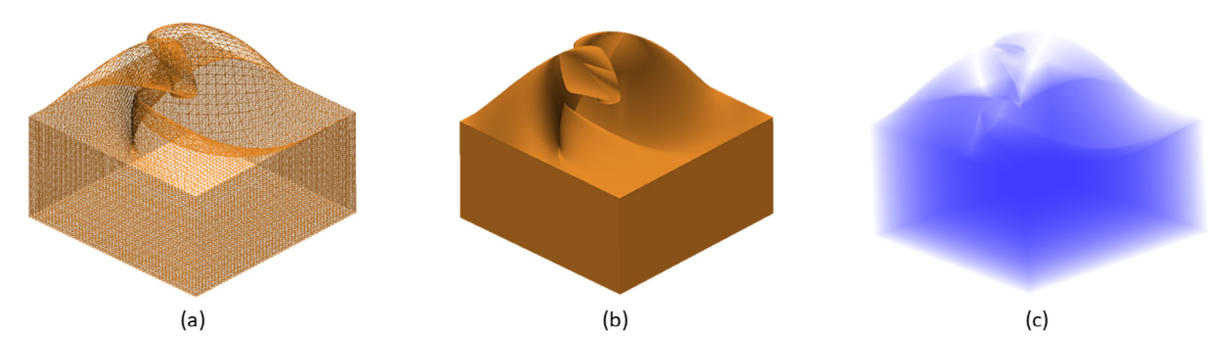


Fig. 12. (a) Wireframe visualization of a solid representation of microstructure generated from NURBS surface. (b) B-rep solid model of the microstructure.(c) Volume rendering of the voxel representation of the microstructure based on point-membership classification of the microstructure.

We next seek to understand the features of the optimized microstructure that results in these dramatic gains. The photocurrent generation process can be thought of as consisting of three steps: light absorption, exciton dissociation, and charge transport. We identify metrics that quantify the performance of each microstructure in terms of these steps [36–38]:

Metric of light absorption: Electron-donor material is responsible for light absorption and exciton generation. Thus, fraction of electron-donor material within the active layer of the device is a natural metric to quantify light absorption (f_{abs}).

Metric of exciton diffusion and dissociation: Generated excitons in the electron-donor material will diffuse towards donoracceptor interface. The bounded electron-hole pair disassociates into free carriers. As a result, an ideal metric to identify exciton diffusion and exciton dissociation is the fraction of dissociated exciton to generated excitons (f_{dis}).

Metric of recombination: The free carriers transport towards the electrodes for collection. However, because of recombination phenomena, collected charges in electrodes are less than generated charges in DA interface. Consequently, fraction of recombined charges to all free charges created in DA interface is a good metric for quantifying recombination (f_{rec}). Since we are interested in amount *not recombined*, we consider our metric to be $1-f_{rec}$.

The comparison of the metrics for the optimized and the BHJ microstructures are shown in Table 1, from which the following observations can be made. NURBS 2D has a higher amount of light absorption compared to BHJ 2D. The recombination for this model is relatively lower than BHJ 2D (possibly because of the lower length of the DA interface of NURBS 2D), while the dissociation metrics for both are similar. Thus, the NURBS 2D microstructure is

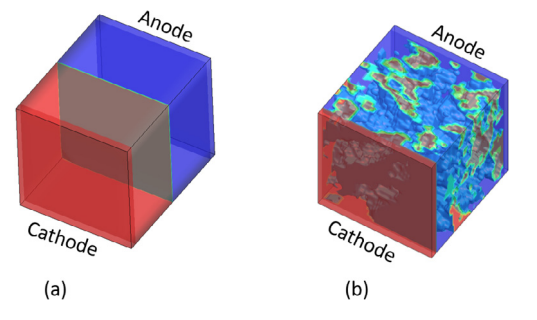


Fig. 13. 3D microstructure of (a) bilayer and (b) bulk heterojunction (BHJ). Red denotes electron acceptor and blue denotes donor regions, respectively. (For interpretation of the references to color in this figure legend, the reader is referred to the web version of this article.)

similar or better in all three metrics than the BHJ 2D microstructure. Light absorption and dissociation of NURBS 3D is slightly lower than that of BHJ 3D, respectively. However, this is more than made up for an excellent recombination metric. This is key insight into designing better microstructures. BHJ microstructures exhibit large recombination losses, which is a good area for improvement. The optimized 3D microstructure essentially only improves recombination losses, but shows no improvement in the other two stages, and yet produces improved short circuit current.

A natural question that arises is the manufacturability of the designed microstructures. As stated earlier, conventional approaches of fabricating OSC thin films involve solution processing

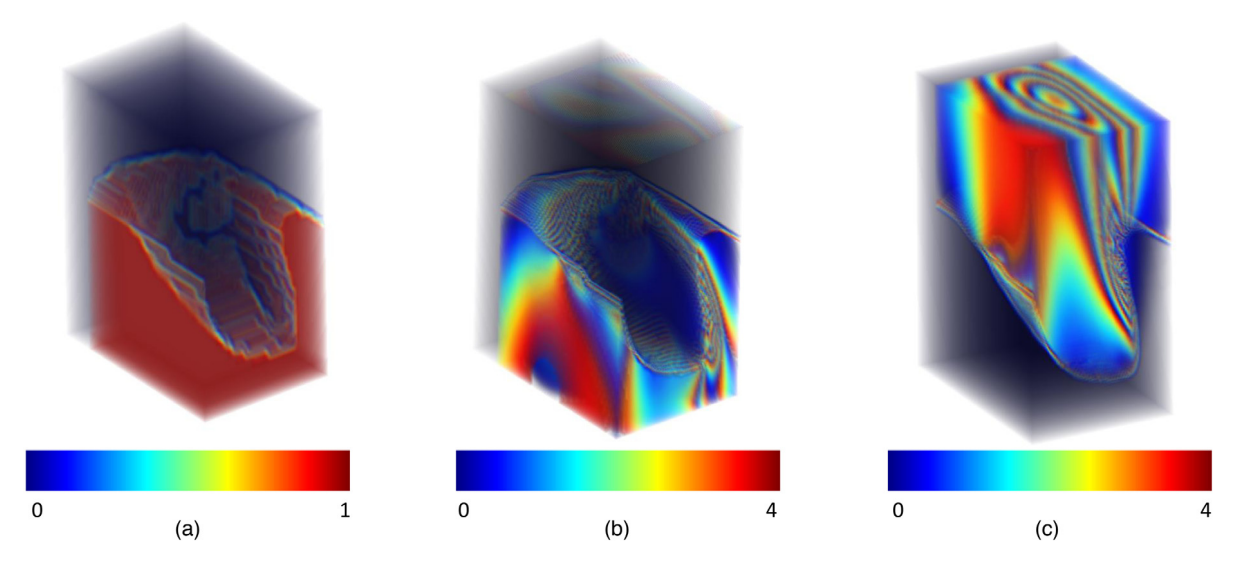


Fig. 14. Optimized microstructure design using NURBS surfaces. (a) Microstructure. red shows electron acceptor regions and blue shows electron donor regions. (b) Normal component of electron current density. (c) Normal component of donor current density. (For interpretation of the references to color in this figure legend, the reader is referred to the web version of this article.)

Table 1 Performance characterization of the optimized microstructures.

Methodology	f_{abs}	f_{dis}	$1-f_{rec}$
BHJ 2D	0.541	0.332	0.462
NURBS 2D	0.760	0.393	0.898
BHJ 3D	0.573	0.449	0.387
NURBS 3D	0.546	0.401	0.934

leverage phenomena like phase-separation and domain coarsening to produce bi-continuous morphologies. Additionally, the use of block co-polymers can produce micro phase-separation producing very fine (and controllable) bi-continuous structures. Speculatively, advances in 3D printing technology suggest even finer control of the morphology opening up the possibility of production of complex tailored DA interfaces. A final remark is worth noting here: the OSC community generally considers two distinct problems in the context of morphology design. The first problem is identification of optimal morphologies without considerations of *reachability* of that morphology by current manufacturing processes. The second problem is the identification of high-performing morphologies within the bounds of processing conditions currently available [39]. The focus of this paper is on the former problem.

The methodology we adopted for optimizing the 3D microstructures can be further fine-tuned. Here we avoided the difficult step of finding the self-intersection in 3D surfaces by computing the lower envelope. As a result, the self-intersected regions do not contribute to the final shape of the microstructure and hence, reduces the complexity of the generated structures. Future work on this topic would explore an exact method to remove self-intersections in 3D, which can lead to a more diverse set of microstructures in 3D

7. Conclusions

Optimizing the microstructure in OSCs can lead to higher photo current generation of the device. In this study we framed the microstructure design optimization problem in terms of designing the interface between the donor and acceptor regions. Donor–acceptor interface was represented using surface and curve modeling techniques. Maximizing the short circuit current generation was performed using meta-heuristic, gradient-free optimization techniques. OSC's current generation was modeled

using the exciton-drift-diffusion (XDD) equations. Our framework works for both 2-D and 3-D structures. Results show substantial improvement in current density compared to the bulk-heterojunction microstructures. Using a surface or curve based technique to model the DA interface reduces the number of design variables and allows the use of sophisticated gradient-free optimization methods to design the OSC microstructure for optimal performance. The proposed surface representation approach seems to be a promising approach for interface design in engineered systems.

Acknowledgments

This work was partly supported by the NSF CMMI, USA grant 1644441 (AK, SG), and NSF DMR, USA grant 1435587 (BG, RN). We also gratefully acknowledge computing resources via XSEDE (Extreme Science and Engineering Discovery Environment), USA and NSF MRI, USA grant 1726447.

Appendix A. Exciton-Drift-Diffusion (XDD) model

In this work, all of the device simulations are performed by using a XDD model, where the electron and hole current densities are shown as:

$$\boldsymbol{J_n} = -qn\mu_n\nabla\varphi + qV_t\mu_n\nabla n\tag{A.1}$$

$$\boldsymbol{J_p} = -qp\mu_p\nabla\varphi - qV_t\mu_p\nabla p \tag{A.2}$$

where q represents the fundamental charge, $V_t = K_bT/q$ is the thermal voltage, K_b is Boltzmann constant and T is temperature. Also φ is the electrostatic potential, while p and n refer to the densities of the electron and hole, and μ_n and μ_p respectively represent the mobility of the electrons and holes. The continuity equations for both carriers are necessary to solve in order to simulate a device such that:

$$\nabla . \boldsymbol{J_n} - R + D = 0 \tag{A.3}$$

$$-\nabla J_{p} - R + D = 0 \tag{A.4}$$

where R is the recombination rate of electrons and holes. The dissociation profile within the most active layer of this device can be found in Eq. (A.6), term D. The carrier continuity equations

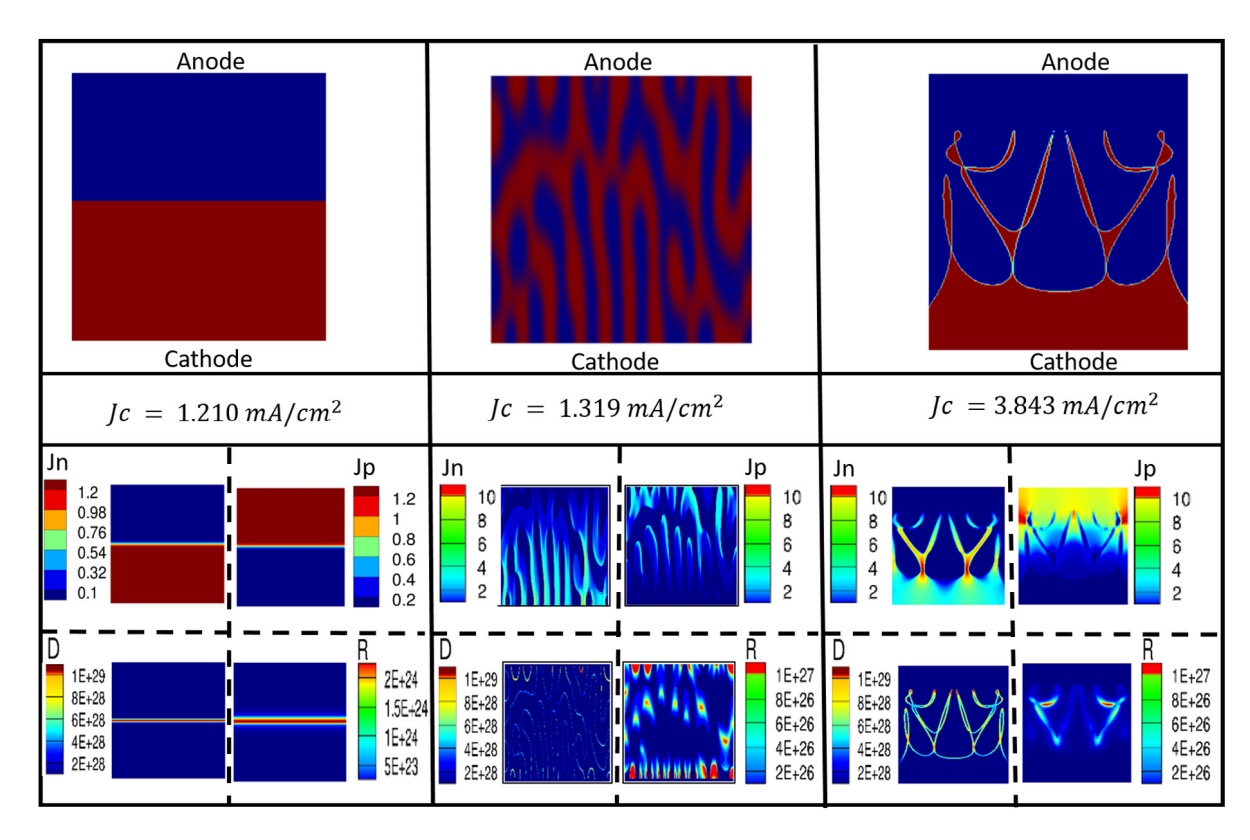


Fig. 15. Performance comparison of 2D optimized microstructure with bilayer and BHJ.

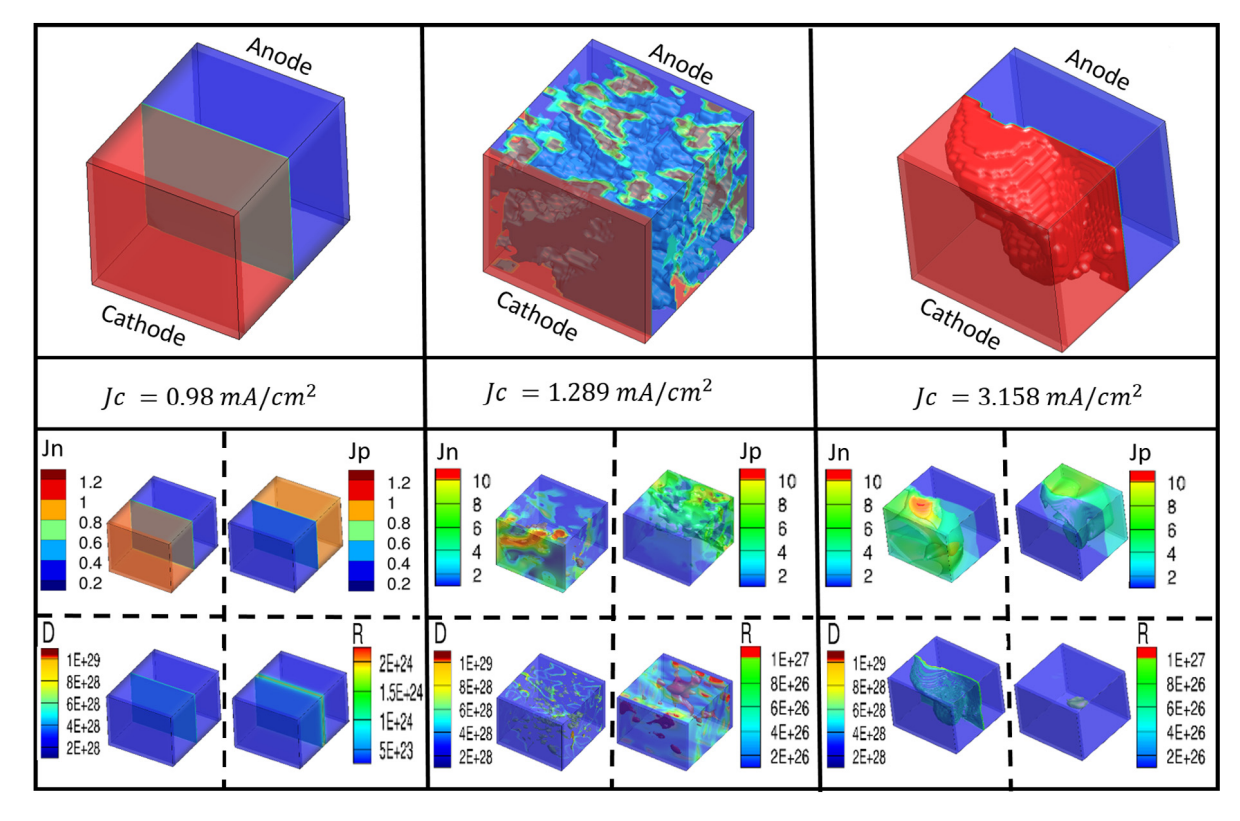


Fig. 16. Performance comparison of 3D optimized microstructure with bilayer and BHJ.

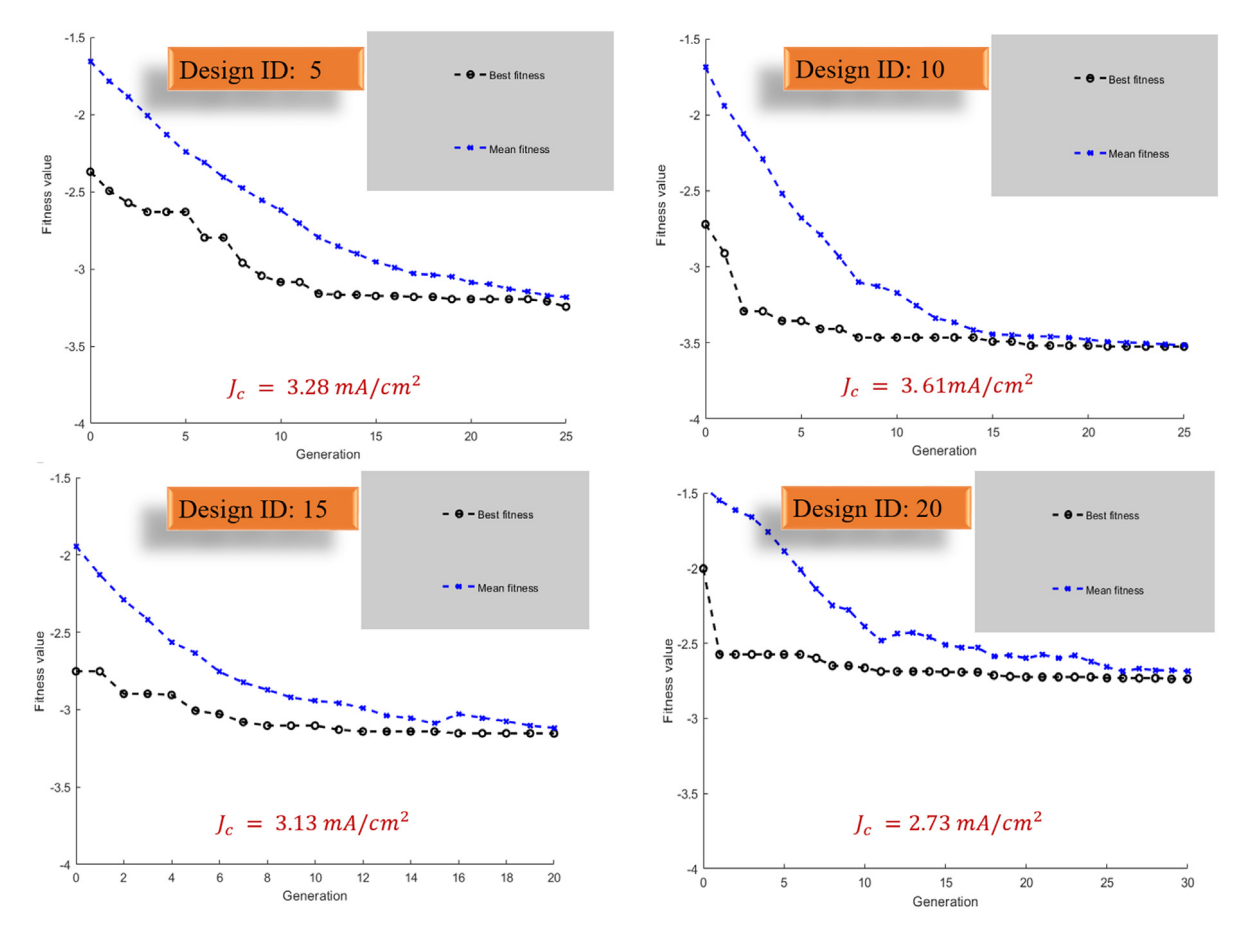


Fig. B.17. GA convergence and current generation for different designs.

need to be coupled through using the following Poisson equation in order to be solved:

$$\nabla .(\epsilon_r \epsilon_0 \nabla \varphi) = q(n-p) \tag{A.5}$$

The vacuum permittivity is represented by ϵ_0 and the dielectric constant of the medium is represented by ϵ_r . For a realistic simulation of an OPV one also need to couple another equation with Eqs. (A.3)–(A.5); this equation is exciton equation. Exciton is directly responsible for dissociation term in drift–diffusion equation such that:

$$D = k_{diss}X \tag{A.6}$$

where $k_{diss} = f(\nabla \varphi)$. Detailed formulation of k_{diss} can be found in Kodali [22]. Exciton (X) is solved such that:

$$-\nabla .(V_t \mu_X \nabla X) - f D_{[\nabla \varphi, X]} - R_{[x]} = -G - R_{[n,p]}$$
(A.7)

The basis of the XDD model is Eqs. (A.3), (A.4), (A.5), and (A.7). Using the Newton method, Eqs. (A.3), (A.4), and (A.5) are solved in an iterative manner and coupled with Eq. (A.7). By discretizing these equations on a finite element mesh, the equations of the XDD model are numerically solved for the active layer.

Appendix B. GA convergence and current generation for different designs

GA is a stochastic optimization method, so it is expected that running it multiple times will produce different results. One practical way to solve this issue is repeating each optimization multiple times. Fig. B.17 samples results from different reruns

of the designs. It can be seen that the different runs result in different optima. We choose the lowest of all the runs as the final result.

References

- [1] Green MA, Emery K, Hishikawa Y, Warta W, Dunlop ED. Solar cell efficiency tables (Version 45). Prog Photovolt, Res Appl 2015;23(1):1–9.
- [2] Vandewal K, Himmelberger S, Salleo A. Structural factors that affect the performance of organic bulk heterojunction solar cells. Macromolecules 2013;46(16):6379–87. http://dx.doi.org/10.1021/ma400924b.
- [3] Servaites J, Ratner M, J. Marks T. Organic solar cells: A new look at traditional models. Energy Environ Sci 2011;4:4410-22. http://dx.doi.org/ 10.1039/C1EE01663F.
- [4] Bagher AM. Comparison of organic solar cells and inorganic solar cells. Int J Sustain Green Energy 2014;3(3):53–8.
- [5] Du P, Zebrowski A, Zola J, Ganapathysubramanian B, Wodo O. Microstructure design using graphs. npj Comput Mater 2018;4(1):50.
 [6] Yanagi H, Tamura N, Taira S, Furuta H, Douko S, Schnurpfeil G, et al.
- [6] Yanagi H, Tamura N, Taira S, Furuta H, Douko S, Schnurpfeil G, et al. An optimal design for photovoltaic properties of two-layer organic solar cells using phthalocyanine and perylene derivatives. Mol Cryst Liq Cryst 1995;267(1):435–40.
- [7] Ray B, Alam MA. Optimum morphology and performance gains of organic solar cells. In: Photovoltaic specialists conference (PVSC), 2011 37th IEEE. IEEE; 2011, p. 003477–81.
- [8] Fullwood DT, Niezgoda SR, Adams BL, Kalidindi SR. Microstructure sensitive design for performance optimization. Prog Mater Sci 2010;55(6):477-562.
- [9] Sundararaghavan V, Zabaras N. Classification and reconstruction of threedimensional microstructures using support vector machines. Comput Mater Sci 2005;32(2):223–39.
- [10] Rosen DW, Jeong N, Wang Y. A method for reverse engineering of material microstructure for heterogeneous CAD. Comput Aided Des 2013;45(7):1068-78.
- [11] Yin Y, Qi R, Zhang H, Xi S, Zhu Y, Liu Z. Microstructure design to improve the efficiency of thermal barrier coatings. Theor Appl Mech Lett 2018;8(1):18–23.

- [12] Zhang L-X, Yang Y-Y. Design and simulation of the metallic microstructures with the controllable reflectivity. Physica B 2019;555:32–5.
- [13] Bhashyam S, Hoon Shin K, Dutta D. An integrated CAD system for design of heterogeneous objects. Rapid Prototyp J 2000;6(2):119–35.
- [14] Wahlborg J, Ganter MA, Schwartz DT, Storti D. H-ism: An implementation of heterogeneous implicit solid modeling. In: ASME 2002 International design engineering technical conferences and computers and information in engineering conference. American Society of Mechanical Engineers; 2002, p. 973–80.
- [15] Kumar V, Burns D, Dutta D, Hoffmann C. A framework for object modeling. Comput Aided Des 1999;31(9):541–56.
- [16] Torquato S. Random heterogeneous materials: microstructure and macroscopic properties, vol. 16. Springer Science & Business Media; 2013.
- [17] Finck BY, Schwartz BJ. Drift-diffusion modeling of the effects of structural disorder and carrier mobility on the performance of organic photovoltaic devices. Phys Rev A 2015;4(3), 034006.
- [18] Finck BY, Schwartz BJ. Drift-diffusion studies of compositional morphology in bulk heterojunctions: The role of the mixed phase in photovoltaic performance. Phys Rev A 2016;6(5). 054008.
- [19] Dantanarayana V, Huang D, Staton J, Moule A, Faller R. Multi-scale modeling of bulk heterojunctions for organic photovoltaic applications. InTech; 2012.
- [20] Jerome J, Ratner M, Servaites J, Shu C-W, Tan S. Simulation of the Buxton-Clarke model for organic photovoltaic cells. In: Computational electronics (IWCE), 2010 14th international workshop on. IEEE; 2010, p. 1–4.
- [21] Buxton GA, Clarke N. Computer simulation of polymer solar cells. Modelling Simul Mater Sci Eng 2006;15(2):13.
- [22] Kodali HK. Simulation based characterization and performance enhancement of heterogeneous polymer solar cells [Ph.D. thesis], Iowa State University; 2013.
- [23] Bazilevs Y, Hughes TJ. Weak imposition of Dirichlet boundary conditions in fluid mechanics. Comput & Fluids 2007;36(1):12–26.
- [24] Lofquist AD. A scalable software framework for solving PDES on distributed octree meshesusing nite element methods scalable software framework for solving pdes on distributed octree meshes using finite element methods [Ph.D. thesis], Iowa State University; 2018.
- [25] Reynolds JR, Thompson BC, Skotheim TA. Conjugated polymers: properties, processing, and applications. CRC Press; 2019.
- [26] Treat ND, Westacott P, Stingelin N. Organic semiconductors: Manipulation and control of the microstructure of active layers. In: The WSPC reference on organic electronics: organic semiconductors: fundamental aspects of materials and applications. World Scientific; 2016, p. 159–93.

- [27] Piegl L, Tiller W. The NURBS book. Springer Science & Business Media; 2012
- [28] Dimitri R, De Lorenzis L, Wriggers P, Zavarise G. NURBS-and T-spline-based isogeometric cohesive zone modeling of interface debonding. Comput Mech 2014;54(2):369–88.
- [29] Chen D, Zhang C. Interface engineering and electrode engineering for organic solar cells. In: Nanostructured solar cells. IntechOpen; 2017, p. 161–81.
- [30] Pach J, Sharir M. On vertical visibility in arrangements of segments and the queue size in the Bentley–Ottmann line sweeping algorithm. SIAM J Comput 1991;20(3):460–70.
- [31] Stoecklein D, Wu C-Y, Kim D, Di Carlo D, Ganapathysubramanian B. Optimization of micropillar sequences for fluid flow sculpting. Phys Fluids 2016;28(1). 012003.
- [32] Wang DH, Kim JK, Park OO, Park JH. Analysis of surface morphological changes in organic photovoltaic devices: bilayer versus bulk-heterojunction. Energy Environ Sci 2011;4(4):1434–9.
- [33] Lu L, Zheng T, Wu Q, Schneider AM, Zhao D, Yu L. Recent advances in bulk heterojunction polymer solar cells. Chem Rev 2015;115(23):12666–731.
- [34] Bingol OR, Krishnamurthy A. NURBS-Python: An open-source objectoriented NURBS modeling framework in Python. SoftwareX 2019;9:85–94. http://dx.doi.org/10.1016/j.softx.2018.12.005.
- [35] Young G, Krishnamurthy A. GPU-accelerated generation and rendering of multi-level voxel representations of solid models. Computers & Graphics 2018;75:11–24.
- [36] Wodo O, Tirthapura S, Chaudhary S, Ganapathysubramanian B. A graph-based formulation for computational characterization of bulk heterojunction morphology. Org Electron 2012;13(6):1105–13.
- [37] Wodo O, Tirthapura S, Chaudhary S, Ganapathysubramanian B. Computational characterization of bulk heterojunction nanomorphology. J Appl Phys 2012;112(6), 064316.
- [38] Wodo O, Zola J, Pokuri BSS, Du P, Ganapathysubramanian B. Automated, high throughput exploration of process-structure-property relationships using the MapReduce paradigm. Mater Discov 2015;1:21–8.
- [39] Pfeifer S, Pokuri BSS, Du P, Ganapathysubramanian B. Process optimization for microstructure-dependent properties in thin film organic electronics. Mater Discov 2018;11:6–13.